EPTT 2024
Escola de Primavera de Transição e Turbulência

ABCM
Associação Brasileira de Engenharia e Ciências Mecânicas

EPTT-2024-0013
A STUDY OF EXPLICIT ALGEBRAIC REYNOLDS STRESS MODELS APPLIED TO AERODYNAMIC FLOWS

Thamires das Chagas Silva
Instituto Tecnológico de Aeronáutica, 12228-900, São José dos Campos, SP, Brazil
th.daschagas@gmail.com

João Luiz F. Azevedo
Instituto de Aeronáutica e Espaço, 12228-904, São José dos Campos, SP, Brazil
joaoluiz.azevedo@gmail.com

Abstract. *This work is part of an ongoing effort to assess the capabilities of nonlinear eddy-viscosity turbulence models to simulate turbulent flows around aeronautical configurations. Nonlinear eddy-viscosity turbulence models are an intermediate class of turbulence models appropriate to work with the Reynolds-averaged Navier-Stokes (RANS) equations. Explicit algebraic Reynolds stress models (EARSMs) are part of this class of turbulence closures. The main advantage of the nonlinear eddy-viscosity turbulence models is the capability to predict the flow more accurately at the same time that keeping the computational cost similar to linear eddy-viscosity turbulence models, which are currently the workhorse of the aeronautical industry. Two EARSMs are employed here, coupled with the 3-D RANS equations. This theoretical formulation is solved in a cell-centered, finite volume method using unstructured meshes. The main applications of interest of this research are flows over high-lift and cruise configurations. The test cases presented in this work include the subsonic flow over the zero pressure gradient flat plate and the transonic flow over the OAT15A airfoil.*

Keywords: *CFD, RANS, Nonlinear Eddy-Viscosity Turbulence Models, Explicit Algebraic Reynolds Stress Models, Turbulence Modeling.*

1. INTRODUCTION

Nowadays, Computational Fluid Dynamics (CFD) results have an important role in most of the aircraft project phases. The Reynolds-averaged Navier-Stokes (RANS) formulation is the methodology typically used by industry to perform these simulations, since the flow analysis should be able to deal with compressible viscous flows. Further, the design of geometries of interest to the industry, such as high-lift and cruise configurations, has to deal with complex physical phenomena present in the flow around these realistic aeronautical shapes. Shock waves, the interaction between shock waves and boundary layers, or flows with separation are examples of complex phenomena very common in such practical industrial applications. In these cases, the theoretical and numerical formulations should be able to represent an accurate solution of the flow, if one has the intention of optimizing such aerodynamic forms.

RANS methodology is a robust and cost-effective approach to capture the mean flow with turbulence effects. Despite its well-known weaknesses, the RANS formulation remains the front-line tool to predict turbulent flows by the aeronautical industry (Gatski *et al.*, 2007). The RANS approach assumes that the flow properties can be decomposed in a time-averaged part plus fluctuations. The mean flow is, then, computed while the fluctuations arising from turbulence are modeled using a so-called turbulence model. This implies that all the turbulence effects are modeled in a cost-efficient manner, making the RANS approach more attractive for the industry due to its low cost. However, this aspect also represents its primary drawback. The turbulence models used in a RANS methodology are concerned with a form to compute the Reynolds stress tensor, which appears as the result of the averaging process and needs to be modeled, bringing back to the solution, at least, the most relevant portion of the effects of turbulence. There are three more relevant classes of turbulence models, named as linear eddy-viscosity models (LEVMs), nonlinear eddy-viscosity turbulence models (NLEVMs), the Reynolds stress models (RSM).

LEVMs are the simplest class of turbulence models, widely adopted by the industry for their capabilities to represent many practical flows with good quality (Carvalho *et al.*, 2018; Bigarella and Azevedo, 2007). LEVMs are based on the

Boussinesq hypothesis, which states that the Reynolds stress tensor is linearly proportional to the strain rate tensor of the mean velocity field. This relation is made through the turbulent eddy-viscosity coefficient, μ_t, correlating the two tensors, the Reynolds stress tensor and the strain rate tensor. The Spalart and Allmaras (1994) and the SST (Menter, 1993) models are well-known examples of this approach. The main drawback of this methodology is that the Boussinesq hypothesis does not allow for the incorporation of anisotropy effects, which are known to exist in the Reynolds stress tensor for many practical applications. Therefore, in cases in which the anisotropy of the turbulent stresses is relevant, such as a boundary layer with an adverse pressure gradient or the interaction between a boundary layer and a shock wave on a transonic wing, the LEVMs become inaccurate.

RSMs solve one transport equation for each component of the Reynolds stress tensor and one transport equation for a characteristic length. This approach considers the anisotropy of the turbulent stresses and, by directly computing each component of the Reynolds stress tensor, it stands for the highest level of possible physical representation among the RANS turbulence models. Examples of such models can be found in Eisfeld *et al.* (2016). Theoretically, RSMs are capable of dealing with complex phenomena and obtaining more accurate results. However, this class of turbulence models requires more refinement in regions close to walls, and obtaining converged solutions for flows around complex geometries are more difficult. Furthermore, solving seven additional transport equations results in a significant increase in computational time, which limits its use by the industry.

NLEVMs represent an intermediate class between the two previously discussed categories and are the primary focus of the present work. This approach allows keeping the computational code structure based on LEVMs while incorporating nonlinear terms in the relation between the Reynolds stress tensor and the strain rate tensor. These nonlinear terms allow the formulation to go beyond the Boussinesq hypothesis and enable the handling of more complex phenomena within a cost similar to that of linear eddy-viscosity turbulence models. Motivated by this background, the present research aims to evaluate the capabilities of nonlinear eddy-viscosity turbulence models in representing turbulent flows for aeronautical applications. Among the methods of obtaining nonlinear eddy-viscosity turbulence models, this work focuses on explicit algebraic Reynolds stress models (EARSMs). EARSMs are constructed as a combination of a LEVM, which provides the linear part of the Reynolds stress tensor, and a constitutive model that computes the anisotropy of the Reynolds stresses. The constitutive model uses nonlinear algebraic terms derived as explicit functions of the strain rate tensor and the rotation rate tensor of the mean flow. This procedure results in a nonlinear turbulence model obtained with a modest increase in computational effort compared to EVMs. The present work addresses two EARSMs, named here as NLBSL (Hellsten, 2005), and a modified version of this model, referred to as NLBSL-V2 (Chagas Silva, 2021; Chagas Silva *et al.*, 2022). Theoretical and numerical formulations, including more details about both nonlinear eddy-viscosity turbulence models under consideration, are described in the following section.

2. THEORETICAL AND NUMERICAL FORMULATIONS

2.1 Reynolds-Averaged Navier-Stokes Equations

The physical model to represent flows of interest in this work is formed by the 3-D compressible RANS equations, and these equations are solved together with an appropriate turbulence model. The 3-D compressible RANS equations, in Cartesian coordinates, can be written as (Bigarella and Azevedo, 2009)

$$\frac{\partial \mathbf{Q}}{\partial t} + \nabla \cdot \left(\mathbf{P}_e - \mathbf{P}_v \right) = 0 \,, \qquad \mathbf{Q} = \begin{bmatrix} \rho & \rho u & \rho v & \rho w & e & \rho \mathcal{T}_1 & \rho \mathcal{T}_2 \end{bmatrix}^T \,, \tag{1}$$

where $\mathbf{Q}$ is the vector of conserved variables that defines the state of the fluid. ρ represents the density of the fluid, u, v and w are the components of the velocity vector, $\mathbf{v}$, respectively, and e is the total energy per unity of volume. The properties $\mathcal{T}_1$ and $\mathcal{T}_2$ represent the turbulent variables, which are defined by the turbulence model. These properties are discussed in the Sec. 2.3 $\mathbf{P}_e$ and $\mathbf{P}_v$ are the inviscid and viscous flux vectors, respectively, defined as

$$\mathbf{P}_e = \begin{Bmatrix} \rho \mathbf{v} \\ \rho u \mathbf{v} + p \hat{\imath}_x \\ \rho v \mathbf{v} + p \hat{\imath}_y \\ \rho w \mathbf{v} + p \hat{\imath}_z \\ (e+p)\mathbf{v} \\ \rho \mathcal{T}_1 \mathbf{v} \\ \rho \mathcal{T}_2 \mathbf{v} \end{Bmatrix} \,, \qquad \mathbf{P}_v = \begin{Bmatrix} 0 \\ (\tau_{xj} + \tau^t_{xj})\ \hat{\imath}_j \\ (\tau_{yj} + \tau^t_{yj})\ \hat{\imath}_j \\ (\tau_{zj} + \tau^t_{zj})\ \hat{\imath}_j \\ \beta_j\ \hat{\imath}_j \\ \mu_{diff_1} \mathcal{T}_{1,j} \hat{\imath}_j \\ \mu_{diff_2} \mathcal{T}_{2,j} \hat{\imath}_j \end{Bmatrix} \,. \tag{2}$$

The static pressure is obtained by the equation of state, $p = (\gamma - 1)\rho e_i$, in which the internal energy is computed by $e_i = c_v T$. Here, γ and c_v are the ratio of specific heats for air and the specific heat at constant volume, respectively. The

shear stress tensor, τ_{ij}, is defined as

$$\tau_{ij} = \mu \left[\left(\frac{\partial u_i}{\partial x_j} + \frac{\partial u_j}{\partial x_i} \right) - \frac{2}{3} \frac{\partial u_m}{\partial x_m} \delta_{ij} \right] , \tag{3}$$

where the molecular viscosity coefficient, μ, is computed by the Sutherland's law (Blazek, 2015). The β_j variable represents the work of the viscous forces and heat transfer term, which is written as $\beta_j = \tau_{ij} u_i - q_j$. The heat conduction vector, q_j, is defined as

$$q_j = -\gamma \left(\frac{\mu}{Pr} + \frac{\mu_t}{Pr_t} \right) \frac{\partial \left(e_i \right)}{\partial x_j} . \tag{4}$$

The Prandtl number, Pr, and the turbulent Prandtl number, Pr_t, are typically assumed as constants in the literature, with values 0.72 and 0.9, respectively, considering the flow conditions which are typical for the applications of this work (Blazek, 2015). The turbulent eddy-viscosity coefficient, μ_t, and the Reynolds stress tensor, τ_{ij}^t, are both modeled by an appropriate turbulence model. The modeling of these properties, μ_t and τ_{ij}, should be able to include the turbulence effects into the RANS equations. The turbulence models employed in this work are discussed with more details in the Sec. 2.3

2.2 Numerical Formulation

The RANS equations are solved in a cell-centered finite volume formulation, written as

$$\frac{\partial \mathbf{Q}_i}{\partial t} = -\frac{1}{V_i} \sum_{k=1}^{nf} \left[\left(\mathbf{P}_{e_k} - \mathbf{P}_{v_k} \right) \cdot \mathbf{S}_k \right] , \tag{5}$$

where the k subscript represents properties computed in the k-th face of the i-th control volume, and nf is the total number of faces of each control volume. $\mathbf{S}_k$ is the area vector of the k-th face and V is the volume of the cell. The derivation of Eq. (5) assumes constant fluxes through volume faces and conserved property constants $\mathbf{Q}_i$ inside the i-th volume. The convective fluxes are discretized by the Roe flux-difference splitting scheme (Roe, 1981), which can be written for the k-th face as

$$\mathbf{P}_{ek} \cdot \mathbf{S}_k = \frac{1}{2} \left[\mathbf{P}_e \left(\mathbf{Q}_L \right) + \mathbf{P}_e \left(\mathbf{Q}_R \right) \right] \cdot \mathbf{S}_k - \frac{1}{2} |\tilde{\mathbf{A}}_k| \left(\mathbf{Q}_R - \mathbf{Q}_L \right) |\mathbf{S}_k| . \tag{6}$$

In Eq. (6), the R and L subscripts indicate the right and left cells to the k-th face, respectively, and $|\tilde{\mathbf{A}}|$ is the Roe matrix. The property values in the k-th face are obtained by a linear reconstruction of the primitive properties at the control volume faces performed using the MUSCL scheme (van Leer, 1979). In regions with strong gradients in the flow, the van Albada limiter function, extended for the multidimensional case (Bigarella and Azevedo, 2012), is used to prevent non-physical oscillations of the solution.

The reconstruction of the viscous flux in the volume faces requires the values of the $\mathbf{Q}$ property gradients at the volume faces. Firstly, the gradients are computed as cell-averaged gradients by the Green-Gauss theorem (Blazek, 2015). Then, the property gradients are extrapolated to the k-th cell faces using a scheme based on Refs. (Blazek, 2015; Cary *et al.*, 2009; Oliveira and Azevedo, 2022), written as

$$\left(\nabla \phi \right)_k = \left(\nabla \phi \right)_{V00} - \left[\left(\nabla \phi \right)_{V00} \cdot \frac{\vec{r}_k}{|\vec{r}_k|} - \frac{\phi_j - \phi_i}{|\vec{r}_k|} \right] \frac{\vec{r}_k}{|\vec{r}_k|} , \qquad \left(\nabla \phi \right)_{V00} = \frac{1}{V_i + V_j} \left(V_i \nabla \phi_i + V_j \nabla \phi_j \right) . \tag{7}$$

In Eq. (7), i and j subscripts represent the cell to the left and the cell to the right of the k-th face, respectively, and $\vec{r}_k$ is the vector connecting the centroids of the cells that share the same k-th face. The symbol ϕ represents a property of the vector of conserved variables, $\mathbf{Q}$. The time march is made with an implicit Euler scheme (Bigarella and Azevedo, 2009) and the linear system is solved by the Restarted Generalized Minimum Residue (GMRES(m)) iterative method (Saad and Schultz, 1986), where the solution os restarted after every m Arnoldi iterations (Oliveira and Azevedo, 2023a). Here, m is taken to be equal to 200 (Oliveira and Azevedo, 2023b).

2.3 Explicit Algebraic Reynolds Stress Models

Turbulence effects are included in the RANS equations by the turbulence model, which is responsible for the modeling of the Reynolds stress tensor, τ_{ij}^t. In EARSMs, the Reynolds stress tensor modeling consists of an eddy-viscosity model

with a constitutive algebraic model to compute the anisotropy of the Reynolds stresses. The two EARSMs addressed in this work use the constitutive algebraic model derived by Wallin and Johansson (2000), which is presented in Sec. 2.3.1 . This constitutive algebraic model is integrated to the eddy-viscosity turbulence model derived by Hellsten (2005). The resulting nonlinear model is labeled here the NLBSL model. A modified version of this model, which is labeled as the NLBSL-V2 turbulence model (Chagas Silva, 2021; Chagas Silva *et al.*, 2022) in the present work, is also addressed in the paper. Both formulations are discussed in the Sec. 2.3.2

2.3.1 The Constitutive Algebraic Model

In EARSMs, usually, the Reynolds stress tensor is written as

$$\tau_{ij}^{t} = 2C_{\mu}^{\mathit{eff}}\rho k\tau S_{ij} - \frac{2}{3}\rho k\delta_{ij} - \rho k a_{ij}^{(ex)} \,, \tag{8}$$

where τ is a characteristic time of the turbulence, S_{ij} is the strain rate tensor, and $a_{ij}^{(ex)}$ is the extra anisotropy tensor. As indicated in Eq. (8), the Reynolds stress tensor is divided into an isotropic and an anisotropic part. The isotropic part is determined by the eddy-viscosity model, although the effective coefficient, C_{μ}^{eff}, is defined by the constitutive model. The extra anisotropic tensor is fully determined by the constitutive model as a function of the strain rate tensor and of the rotation rate tensor, S_{ij} and Ω_{ij}, respectively. The most general form to write the anisotropy tensor as a function of S_{ij} and Ω_{ij} consists of ten tensorially independent groups, in which all higher-order tensor combinations can be reduced with the aid of the Caley-Hamilton theorem (Wallin and Johansson, 2000). Using tensorial notation, the anisotropy tensor is written as

$$\begin{aligned}
\mathbf{a} = {} & \beta_1\tilde{\mathbf{S}} + \beta_2\left(\tilde{\mathbf{S}^2} - \frac{1}{3}II_S\mathbf{I}\right) + \beta_3\left(\tilde{\mathbf{\Omega}}^2 - \frac{1}{3}II_\Omega\mathbf{I}\right) + \beta_4\left(\tilde{\mathbf{S}}\tilde{\mathbf{\Omega}} - \tilde{\mathbf{\Omega}}\tilde{\mathbf{S}}\right) \\
& + \beta_5\left(\tilde{\mathbf{S}^2}\tilde{\mathbf{\Omega}} - \tilde{\mathbf{\Omega}}\tilde{\mathbf{S}^2}\right) + \beta_6\left(\tilde{\mathbf{S}}\tilde{\mathbf{\Omega}}^2 + \tilde{\mathbf{\Omega}}^2\tilde{\mathbf{S}} - \frac{2}{3}IV\,\mathbf{I}\right) + \beta_7\left(\tilde{\mathbf{S}^2}\tilde{\mathbf{\Omega}}^2 + \tilde{\mathbf{\Omega}}^2\tilde{\mathbf{S}^2} - \frac{2}{3}V\,\mathbf{I}\right) \\
& + \beta_8\left(\tilde{\mathbf{S}}\tilde{\mathbf{\Omega}}\tilde{\mathbf{S}^2} - \tilde{\mathbf{S}^2}\tilde{\mathbf{\Omega}}\tilde{\mathbf{S}}\right) + \beta_9\left(\tilde{\mathbf{\Omega}}\tilde{\mathbf{S}}\tilde{\mathbf{\Omega}}^2 - \tilde{\mathbf{\Omega}}^2\tilde{\mathbf{S}}\tilde{\mathbf{\Omega}}\right) + \beta_{10}\left(\tilde{\mathbf{\Omega}}\tilde{\mathbf{S}^2}\tilde{\mathbf{\Omega}}^2 - \tilde{\mathbf{\Omega}}^2\tilde{\mathbf{S}^2}\tilde{\mathbf{\Omega}}\right) \,,
\end{aligned} \tag{9}$$

where $\tilde{\mathbf{S}} = \tau\mathbf{S}$, $\tilde{\mathbf{\Omega}} = \tau\mathbf{\Omega}$, and $\mathbf{I}$ is the identity tensor. The β coefficients are defined in terms of the five independent invariants,

$$II_S = \mathrm{tr}\{\tilde{\mathbf{S}^2}\}, \quad II_\Omega = \mathrm{tr}\{\tilde{\mathbf{\Omega}}^2\}, \quad III_S = \mathrm{tr}\{\tilde{\mathbf{S}^3}\}, \quad IV = \mathrm{tr}\{\tilde{\mathbf{S}}\tilde{\mathbf{\Omega}}^2\}, \quad V = \mathrm{tr}\{\tilde{\mathbf{S}^2}\tilde{\mathbf{\Omega}}^2\} \,, \tag{10}$$

where tr{ } denotes the trace of the tensor. Then, it is necessary to determine the β coefficients to obtain an explicit solution of Eq. (9). Wallin and Johansson (2000) obtained an explicit solution for the 3-D case reducing the anisotropy tensor to five tensorially independent groups, which are those related to the following β coefficients,

$$\begin{aligned}
&\beta_1 = -\frac{N(2N^2 - 7II_\Omega)}{\mathscr{Q}}, \quad \beta_3 = -\frac{12N^{-1}IV}{\mathscr{Q}}, \\
&\beta_4 = -\frac{2(N^2 - 2II_\Omega)}{\mathscr{Q}}, \quad \beta_6 = -\frac{6N}{\mathscr{Q}}, \quad \beta_9 = \frac{6}{\mathscr{Q}} \,,
\end{aligned} \tag{11}$$

and all others β coefficients are identically null. The expressions of N and $\mathscr{Q}$ for the 3-D case can be found in the Refs. (Wallin and Johansson, 2000; Hellsten, 2005). The anisotropic contribution, $a_{ij}^{(ex)}$, is given by Eqs. (9) and (11), with the subtraction of the isotropic part, and is expressed in tensorial notation as

$$\begin{aligned}
\mathbf{a}^{(ex)} = {} & \beta_3\left(\tilde{\mathbf{\Omega}}^2 - \frac{1}{3}II_\Omega\mathbf{I}\right) + \beta_4\left(\tilde{\mathbf{S}}\tilde{\mathbf{\Omega}} - \tilde{\mathbf{\Omega}}\tilde{\mathbf{S}}\right) \\
& + \beta_6\left(\tilde{\mathbf{S}}\tilde{\mathbf{\Omega}}^2 + \tilde{\mathbf{\Omega}}^2\tilde{\mathbf{S}} - II_\Omega\tilde{\mathbf{S}} - \frac{2}{3}IV\mathbf{I}\right) + \beta_9\left(\tilde{\mathbf{\Omega}}\tilde{\mathbf{S}}\tilde{\mathbf{\Omega}}^2 - \tilde{\mathbf{\Omega}}^2\tilde{\mathbf{S}}\tilde{\mathbf{\Omega}}\right) \,.
\end{aligned} \tag{12}$$

The model defines the effective coefficient present in Eq. (8) as $C_{\mu}^{eff} = -\frac{1}{2}\left(\beta_1 + II_\Omega\beta_6\right)$. In the present case, then, this coefficient is a variable rather than a constant value. Actually, the value typically used in linear eddy-viscosity two-equation turbulence models is $C_\mu = 0.09$. This constitutive model presented here is used in both EARSMs addressed in this work, the NLBSL and the NLBSL-V2 turbulence models.

2.3.2 Coupling with the Eddy-Viscosity Model

The constitutive model presented in the previous section is coupled to the eddy-viscosity model calibrated by Hellsten (2005). Together, these formulations result in the nonlinear eddy-viscosity turbulence model referred to here as the NLBSL model. The eddy-viscosity model calibrated by Hellsten is a two-equation turbulence model, which was obtained from the k-ω model known as the BSL model (Menter, 1993). The two transport equations are written as

$$\begin{aligned}
&\frac{\partial(\rho k)}{\partial t} + \frac{\partial(\rho u_j k)}{\partial x_j} = P_k - \beta^* \rho \omega k + \frac{\partial}{\partial x_j}\left[(\mu + \sigma_k \mu_t)\frac{\partial k}{\partial x_j}\right], \\
&\frac{\partial(\rho \omega)}{\partial t} + \frac{\partial(\rho u_j \omega)}{\partial x_j} = \gamma \frac{\omega}{k} P_k - \beta \rho \omega^2 + \frac{\partial}{\partial x_j}\left[(\mu + \sigma_\omega \mu_t)\frac{\partial \omega}{\partial x_j}\right] + \sigma_d \frac{1}{\omega} \max\left(\frac{\partial k}{\partial x_j}\frac{\partial \omega}{\partial x_j}; 0\right),
\end{aligned} \tag{13}$$

where the first equation is solved for the mean turbulent kinetic energy, k, and the second equation for the turbulence dissipation rate, ω. The production term of mean turbulent kinetic energy, P_k, is calculated as

$$P_k = \tau_{ij}^t \frac{\partial u_i}{\partial x_j}, \tag{14}$$

where the Reynolds stress tensor, τ_{ij}^t, is defined in Eq. (8). The constants of the model are computed through the transfer function defined as

$$F_1 = \tanh(1.5\text{arg}_1^4), \tag{15}$$

$$\text{arg}_1 = \min\left[\max\left(\frac{\sqrt{k}}{\beta^* \omega d}; \frac{500\nu}{d^2\omega}\right); \text{arg}_2\right], \tag{16}$$

$$\text{arg}_2 = \frac{20k}{\max\left[d^2\left(\nabla k \cdot \nabla \omega\right)/\omega;\ 200k_\infty\right]}, \tag{17}$$

in such a way that any constant, ϕ, is obtained by $\phi = F_1\phi_1 + (1 - F_1)\phi_2$. The NLBSL model was calibrated with the following constant values

$$\begin{aligned}
&\beta_1 = 0.0747, \quad \sigma_{k1} = 1.1 \quad \sigma_{\omega 1} = 0.53 \quad \gamma_1 = 0.518 \quad \sigma_{d1} = 1.0 \\
&\beta_2 = 0.0828, \quad \sigma_{k2} = 1.1 \quad \sigma_{\omega 2} = 1.0 \quad \gamma_2 = 0.44 \quad \sigma_{d2} = 0.4,
\end{aligned} \tag{18}$$

and $\beta^* = 0.09$ in Eq. (13). Finally, the turbulent eddy-viscosity coefficient, μ_t, is computed as $\mu_t = C_\mu^{eff} \rho k \tau$. The coupling between the constitutive model discussed in the Sec. 2.3.1and the formulation presented above consists in the EARSM labeled here as NLBSL turbulence model, which is the model originally calibrated by Hellsten (2005).

The NLBSL model was developed with an interest in high-lift flows. However, the presence of shock waves is typical in aeronautical applications, indicating that compressibility effects are strongly present in the flow. Based on past research (Bigarella and Azevedo, 2007, 2009), a modification was proposed in the original NLBSL model to make it more sensitive to compressibility effects. Usually, the k-ω turbulence models define μ_t as proportional to k/ω. For example, in the BSL model, $\mu_t = \rho k/\omega$. The original NLBSL model multiplies the production term in the ω transport equation by ω/k, Eq. (13). Considering the common definition of μ_t in linear eddy-viscosity turbulence models, this is similar to dividing the production term in the ω equation by ν_t. This approach is precisely the selection implemented in the SST model, in which the production term in the ω equation is divided directly by the ν_t coefficient. Therefore, this modification was implemented in the original NLBSL formulation, resulting in the ω equation rewritten as

$$\frac{\partial(\rho \omega)}{\partial t} + \frac{\partial(\rho u_j \omega)}{\partial x_j} = \gamma \frac{P_k}{\nu_t} - \beta \rho \omega^2 + \frac{\partial}{\partial x_j}\left[(\mu + \sigma_\omega \mu_t)\frac{\partial \omega}{\partial x_j}\right] + \sigma_d \frac{1}{\omega} \max\left(\frac{\partial k}{\partial x_j}\frac{\partial \omega}{\partial x_j}; 0\right). \tag{19}$$

Hence, the only difference between this equation and the ω equation from the original NLBSL model, Eq. (13), is in the production term. For the ω equation written as in Eq. (19), the EARSM is addressed in this work as NLBSL-V2 model.

3. RESULTS AND DISCUSSION

The test cases that have been addressed so far in the present investigation include the subsonic flow over a flat plate and the transonic flow over an OAT15A airfoil. The results were obtained with an in-house CFD code that can only handle three-dimensional grids. Thus, all the 2-D test cases are 2-D geometries with one extruded control volume in the spanwise direction. This is an appropriate practice because, for the cases addressed here, there are no expectations that 3-D effects will be relevant to the solutions. For all test cases, flow conditions use no transition modeling or specification of transition location, *i.e.*, the flow is considered fully turbulent.

3.1 Verification Case: Zero Pressure Gradient Flat Plate

The first case discussed here is the subsonic flow over the zero pressure gradient flat plate, addressed as a verification case by NASA Langley Research Center in the turbulence modeling resource (TMR) web page (Rumsey, 2024). The flow over the plate has a Reynolds number of $Re = 5 \times 10^6$, based on a unit of length. The boundary conditions are a freestream Mach number of 0.2 at a temperature of $300K$. The ratio between the stagnation pressure and the reference static pressure at the inflow condition is $P_t/p_{ref} = 1.02828$. Similarly, the dimensionless inflow stagnation temperature is $T_t/T_{ref} = 1.008$. The outflow static pressure ratio is $p/p_{ref} = 1.0$. The flat plate is set as an adiabatic wall with non-slip condition.

This test case has the purpose of verifying the implementation of the nonlinear eddy-viscosity turbulence models. Only the NLBSL model results are shown for code verification purposes because there is no significant difference between the implementations of NLBSL and NLBSL-V2 turbulence models. The results are compared to solutions obtained by the CFL3D NASA code using a version of the SST turbulence model, named at the TMR web page as SST-Vm model (Rumsey, 2024). The web page does not have results from the NLBSL or NLBSL-V2 models available for this case. Since the objective of this study case is just to verify the implementation of the turbulence model, the comparison between these two different turbulence models is sufficient for it. The meshes used are 3-D hexahedral grids also from the TMR web page, with approximately 12000, 53000 and 209000 cells.

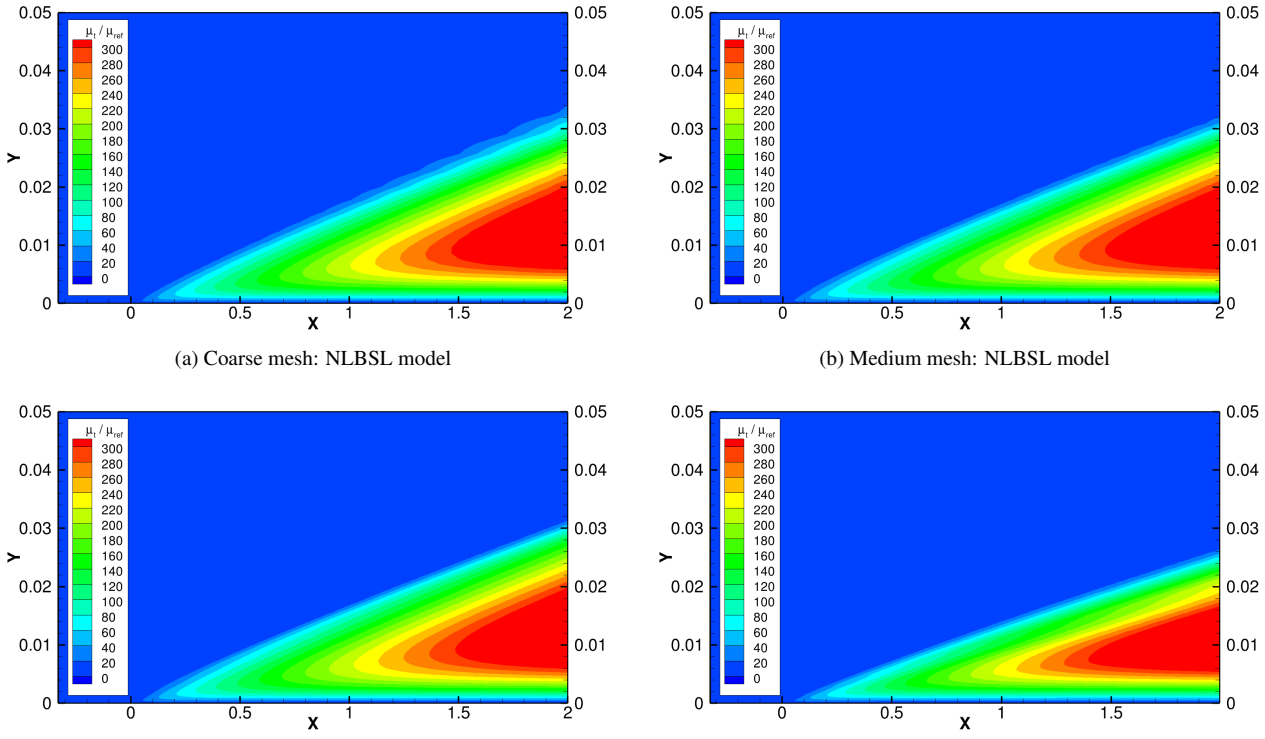

(a) Coarse mesh: NLBSL model

(b) Medium mesh: NLBSL model

(c) Fine mesh: NLBSL model

(d) Fine mesh: CFL3D Results

Figure 1: Results for the μ_t/μ field for the flat plate. The NLBSL solutions are compared with the CFL3D solution for implementation verification.

Figure 1 shows the contours of the turbulent eddy-viscosity coefficient near the leading edge of the plate for the three mesh levels and the reference results from the CFL3D code. By analyzing the contours, it is seen that the production of the turbulent eddy-viscosity coefficient along the flat plate yields μ_t values which are 300 times larger than the molecular viscosity coefficient. In Figs. 1a, 1b and 1c, respectively, it is observed that there exists a mesh dependency in the solution. The result obtained with the coarse mesh shows a large diffusion of the μ_t production, but, while refining the mesh, the production field becomes better defined. When comparing the results from the NLBSL turbulence model with the reference results, both obtained with the fine mesh, Figs. 1c and 1d, respectively, the region with a significative production of μ_t is thicker in the result computed with the nonlinear turbulence model. Since the definition of μ_t is not the same for the turbulence models used to compute these results, it is not completely surprising that there are slight differences in the contour distributions for the properties of the flow.

As stated, it should be understood that the turbulence model available in the CFL3D code is different from the NLBSL model. Furthermore, although the numerical methods available in the CFL code have similarities with those used in the BRU3D code, the numerics on the two codes are indeed different, despite the fact that both codes are 2nd order accurate.

Therefore, there are differences on the theoretical formulations of the models used and on the numerical formulations implemented in the two codes. These are important points to highlight as both physical and numerical modeling from computational tools can affect the final solution, despite the fact that both CFD codes achieve second order accuracy. One possible outcome of these differences is precisely the larger spreading of the μ_t contours seen in the present flow visualizations. However, despite these comments, the results have qualitatively good agreement, and this is the sort of comparison that one can reasonably expect from this verification case.

Figure 2 illustrates the theoretical logarithmic law of the wall and the solution from the NLBSL turbulence model at two positions along the plate. The dashed curve is given by

$$u^+ = \frac{1}{\kappa} \ln y^+ + B \,, \tag{20}$$

where κ is the von Kárman constant, $\kappa = 0.41$, and B is a constant given as $B = 5.0$ (Pope, 2000). The red curve represents the velocity profile roughly in the middle of the plate and the blue curve is the velocity profile at the end of the plate. As expected, the viscous sublayer region, $y^+ < 5$, is very well represented by the present solutions. This region of the flow is dominated by the molecular viscosity, so the turbulence model should not affect the solution of this sublayer. In the viscous wall region, i.e., while $y^+ < 50$, the molecular viscosity is still significant. For the log-law region, $y^+ > 30$, the velocity profiles follow the logarithmic law. Outside the viscous wall region, $y^+ > 50$, the molecular effects are negligible because the flow became fully turbulent. In this region, the total stress tensor is obtained essentially from the turbulence model, therefore having only the turbulent stresses contribution. As one can see in Fig. 2, the present results have a very good agreement with the law of the wall in the logarithmic portion of the boundary layer. Based on these results, the authors consider that the implementation of the NLBSL and NLBSL-V2 turbulence models was successful.

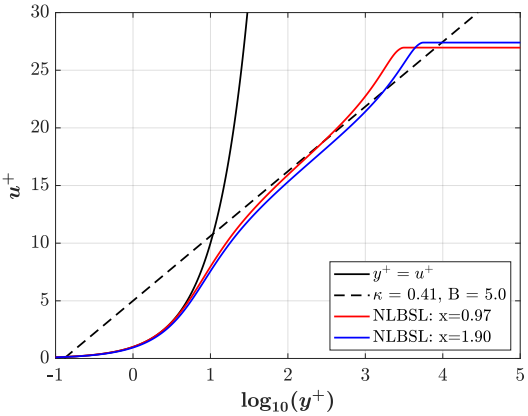

Figure 2: Logarithmic law of the wall and velocity profiles obtained with the NLBSL turbulence model. The velocity profiles are from two different locations along the plate.

3.2 Transonic Flow over OAT15A Airfoil

This test case is the transonic flow over the OAT15A airfoil, labeled in Ref. (Roddle and Archambaud, 1994) as case A-11. The flow conditions are $Re = 3 \times 10^6$ based on the airfoil chord of 1 m of length, a freestream Mach number of 0.724, the air temperature of 246.66 K, and the airfoil angle of attack is 1.15 deg. With these flow conditions, the main aerodynamic phenomena are the shock wave on the upper surface of the airfoil and the interaction between this shock and the boundary layer. Figure 3 shows the three hexahedral mesh levels used in this study. These grids were built according to experience from past research of the group. They have a global refinement factor of 1.5 between each mesh level and a 1.1 growth factor in the normal direction. The nomenclature 100×100 cells in the coarse mesh, Fig. 3a, means there are 100 cells both along the airfoil and the normal direction. The same is valid for the other meshes illustrated in the Figs. 3b and 3c, respectively. The external boundary is located at 120 chords from the airfoil in the three meshes.

In addition to the reference experimental data (Roddle and Archambaud, 1994), the results obtained with the nonlinear turbulence models are compared with results from a version of the SST turbulence model previously implemented in the code (Carvalho *et al.*, 2019). This version of the SST model is referred to in the TMR website as the SST-2003 turbulence model (Rumsey, 2024). The comparison between results from linear and nonlinear eddy-viscosity models has the objective of assessing the capabilities of both approaches in representing the solution of this test case.

Tables 1 and 2 show the aerodynamic coefficients obtained with the three turbulence models. The experimental data for this flow condition do not provide reference values of the aerodynamic coefficients, so these data are compared only between the numerical solutions. The column to the right side of the results of each turbulence model indicates

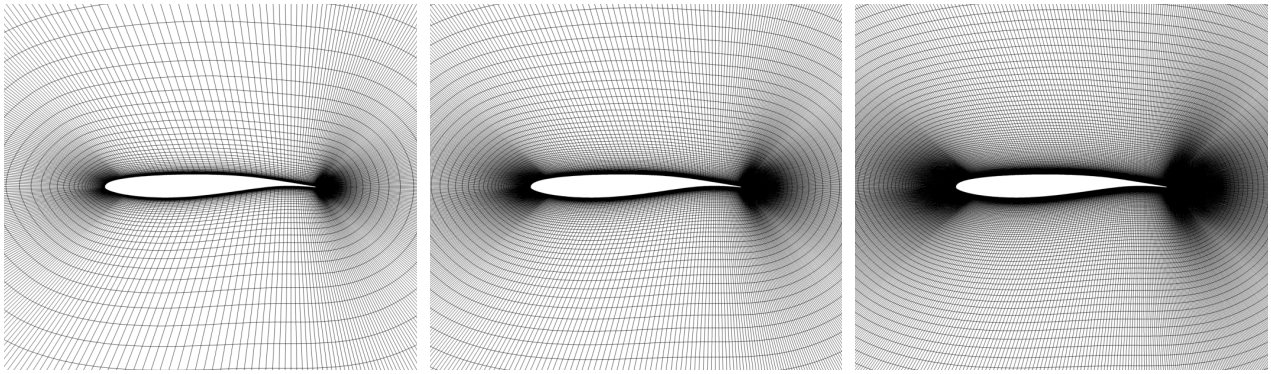

(a) Coarse mesh: 100×100 cells. (b) Medium mesh: 150×150 cells. (c) Fine mesh: 225×225 cells.

Figure 3: Grids used for the OAT15A airfoil simulations.

Table 1: Lift coefficients (C_L) obtained for the OAT15A airfoil case.

Mesh Level	SST	$\%_{\text{SST}}$	NLBSL	$\%_{\text{NLBSL}}$	NLBSL-V2	$\%_{\text{NLBSL-V2}}$
Coarse	0.69172	-	0.68761	-	0.66506	-
Medium	0.69113	0.085	0.68634	0.185	0.66243	0.395
Fine	0.69134	0.030	0.68611	0.034	0.66143	0.151

Table 2: Drag coefficients (C_D) obtained for the OAT15A airfoil case. Values in counts.

Mesh Level	SST	$\%_{\text{SST}}$	NLBSL	$\%_{\text{NLBSL}}$	NLBSL-V2	$\%_{\text{NLBSL-V2}}$
Coarse	127.11	-	128.84	-	122.12	-
Medium	121.58	4.351	123.39	4.230	116.51	4.594
Fine	119.29	1.884	121.22	1.759	114.24	1.948

the variation in the calculated values of the aerodynamic coefficients between two consecutive levels of mesh refinement. Looking at the results of the SST and NLBSL models, the variations in the values of C_L between medium and fine meshes are insignificant, lower than 0.04%. The NLBSL-V2 results present a slightly larger variation, approximately 0.15%, but still remain very small. For the drag coefficients, the value variations for the three turbulence models are lower than 2% between the medium and fine meshes. It is clear from the results in Tabs. 1 and 2 that, with the grid refinement performed, mesh independence has not yet been achieved. However, the changes in the aerodynamic coefficients are considered very small and, given the purpose of this test case, the fine mesh is considered sufficiently refined to proceed with the present investigations. It is important to observe from Tabs. 1 and 2 that the turbulence models converge to different values of the aerodynamic coefficients. This behavior is somewhat expected because, as discussed in the previous case, the turbulence model is part of the physical formulation. Therefore, the solutions from each model could be different.

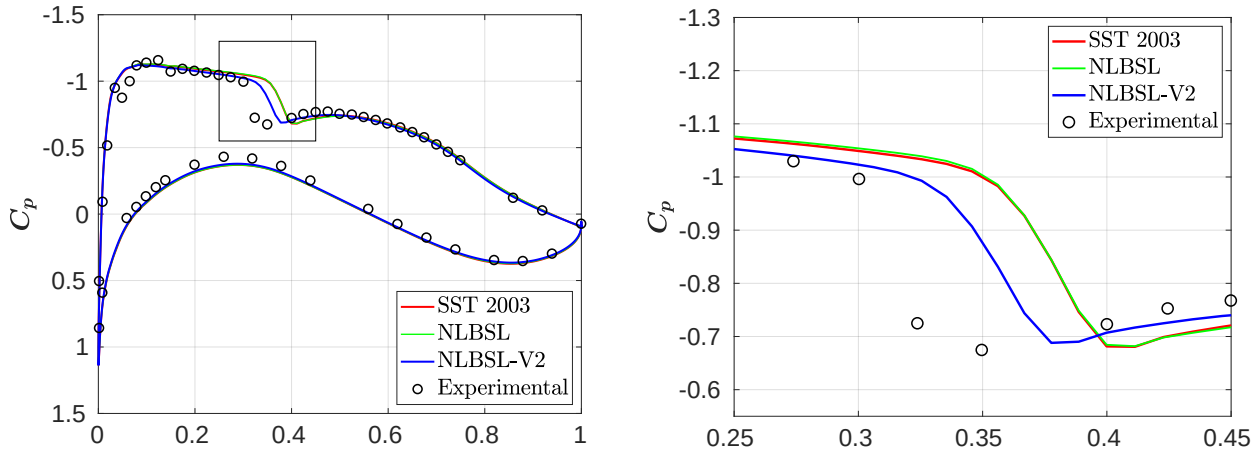

(a) View of the entire airfoil. (b) Zoomed-in view of the shock region.

Figure 4: Pressure coefficient distributions over the OAT15A airfoil.

Figure 4 shows the pressure coefficient distributions of each turbulence model over the airfoil, comparing them with the experimental data. The square drawn in the Fig. 4a highlights the shock wave region, which is displayed in an enlarged view in Fig. 4b. On the lower surface of the airfoil, the three turbulence models have virtually the same representation of the pressure coefficients, although there exist small differences from the experimental data. On the upper surface, the results obtained with the different turbulence models are again very similar, except for the shock wave region. As expected, the transition close to the leading edge is not captured by any turbulence model since the simulations are run considering fully turbulent flow.

Looking at the SST and NLBSL turbulence model results, red and green curves, respectively, the solutions are very close to each other over all regions of the airfoil. The NLBSL model was derived from the BSL model, an earlier version of the SST model and, originally, it was developed for high-lift flows. In such conditions, the freestream flow has a relatively low speed, so the compressibility effects are smaller than in a transonic flow. Hence, this can be an indication of why the NLBSL model has a behavior similar to the SST model in this case. It is important to note that during the development of a turbulence model, the model constants are determined by evaluating the model results for a set of test cases, resulting in a model that works very well with cases for which physical phenomena are similar to the ones used to calibrate the model constants. Therefore, since the NLBSL model was not originally calibrated for strong compressibility effects, its behavior is consistent with the fact that it may be missing a key part of the physics present in this flow.

The solution obtained with the NLBSL-V2 turbulence model, the blue curve, shows that this model has better capabilities to deal with compressibility effects. Its results are in better agreement with the experimental data, particularly in the shock region. This behavior seems to indicate that the modification made in the production term of the ω equation, from the original NLBSL model, becoming the NLBSL-V2 turbulence closure, produced a significant improvement in the ability of the model to deal with transonic flows by making it more sensitive to compressibility effects. Both turbulence models, NLBSL and NLBSL-V2, are characterized as advanced models, considering an anisotropic formulation together with compressibility effects. However, looking at the results from NLBSL and NLBSL-V2 turbulence models, the compressibility effects are predominant over the anisotropy effects in this flow, since NLBSL also has an anisotropic formulation but was not able to capture the shock wave location with more accuracy than the SST model solution.

Given these results, the NLBSL-V2 model is the nonlinear eddy-viscosity turbulence model more appropriate for this case. Therefore, a more detailed analysis between this closure and the SST turbulence model is performed. Figure 5 shows the mean turbulent kinetic energy field, ρk [J/m^3], around the airfoil obtained with the NLBSL-V2 turbulence model. Three specific regions are drawn for a more detailed comparison between the results from SST and NLBSL-V2 models.

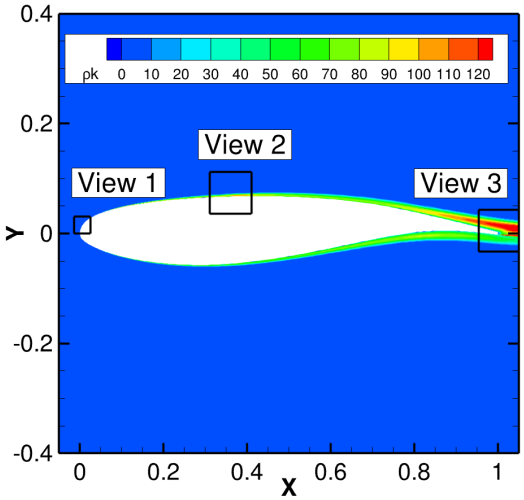

Figure 5: Field of ρk around the OAT15A airfoil obtained with the NLBSL-V2 model. Three specific regions are identified for analysis.

Figure 6 illustrates an enlarged visualization of the view 1 region from Fig. 5. In this region of the flow, which is near the leading edge of the airfoil, it is possible to identify a layer around the airfoil where there is a significant production of the mean turbulent kinetic energy. The objective of highlighting this region is to see how each turbulence model predicts the ρk field and how this affects the solution of the flow. The circles in Figs. 6a and 6b indicate the beginning of the more rapid growth of the boundary layer. The beginning of this region computed with the SST turbulence model is further upstream than with the NLBSL-V2 solution. Moreover, the ρk layer formed around the airfoil is slightly thicker in the SST solution than in the NLBSL-V2 model results.

Figure 7 shows the view 2 region from Fig. 5. The dashed lines indicate the rough location of the shock wave captured

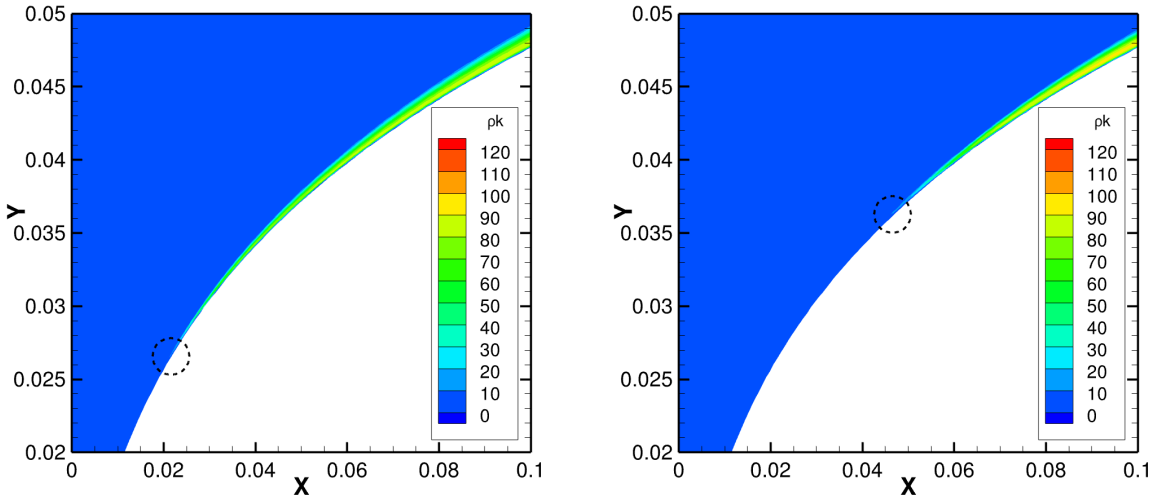

(a) SST (b) NLBSL-V2

Figure 6: Results for the ρk field around the OAT15A airfoil leading edge. View 1 region from Fig. 5.

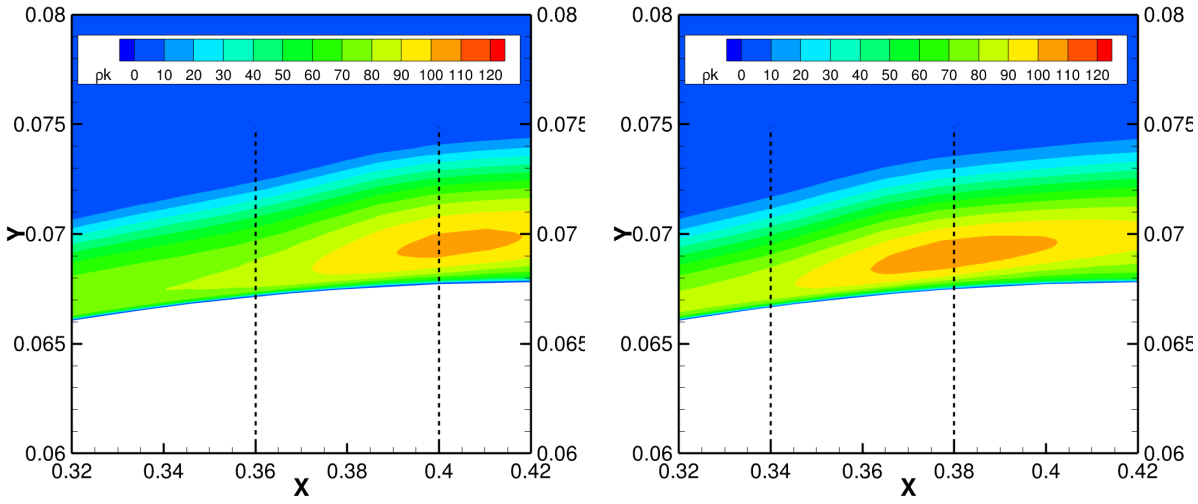

(a) SST (b) NLBSL-V2

Figure 7: Results for the ρk field around the OAT15A airfoil upper surface shock location. View 2 region from Fig. 5.

by each turbulence model. The layer with significant production of mean turbulent kinetic energy near the shock wave is thicker in the SST solution than in the NLBSL-V2 solution. One can see that the highest values of ρk occur in the downstream portion of the region where the shock impinges upon the boundary layer. The boundary layer with higher turbulence levels seems to position the shock wave further downstream. Another aspect that deserves to be remembered is that the observed behavior can also be related to the known characteristic of linear turbulence models of computing larger turbulence levels around the shock wave region. This can be observed by the yellow area in Fig. 7, indicating that there is a larger concentration of mean turbulent kinetic energy slightly after the shock in the SST solution.

Figure 8 shows the view 3 region from Fig. 5, which is the airfoil trailing edge region. A larger "spread" of higher levels of turbulent kinetic energy can be observed in the NLBSL-V2 model solution. Despite this, the maximum value of turbulent kinetic energy in the entire field is computed by the SST model. This maximum value of ρk occurs near the trailing edge of the airfoil, reaching approximately 172 J/m^3, whereas the maximum value of ρk computed by the NLBSL-V2 model is approximately 126 J/m^3.

The results presented in the transonic flow over OAT15A airfoil show that the use of a nonlinear eddy-viscosity model has a very significant positive effect on the final solution. Additionally, there is one important point to consider. For industrial applications, it is crucial to achieve a good balance between accurate solutions and computational cost. Table 3 presents a relative computational cost estimate for the three turbulence models, considering the simulations of the flow over the OAT15A airfoil using only the fine mesh and running 50000 iterations. The data presented in Table 3 were obtained by actually measuring CPU time using features of the operating system in which the test case was run. Therefore, this is a true comparison of the relative computational costs of the different turbulence models. It can be observed that there exists

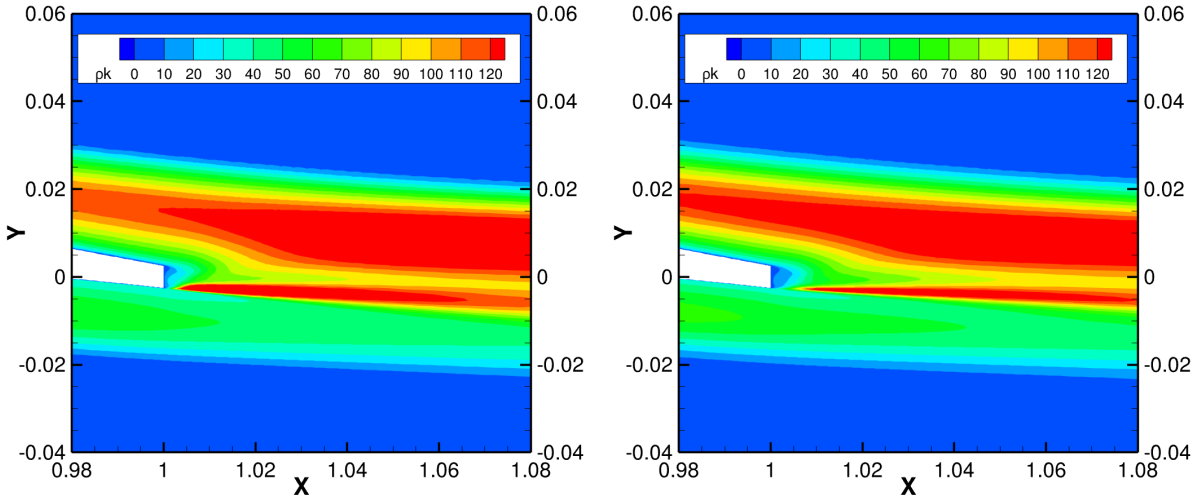

(a) SST (b) NLBSL-V2

Figure 8: Results for the ρk field around the OAT15A airfoil trailing edge. View 3 region from Fig. 5.

an additional cost for the nonlinear eddy-viscosity turbulence models compared to the linear eddy-viscosity turbulence model. Some extra cost is expected because nonlinear relations were included in these models. However, considering the fairly significant improvement in the results obtained with the NLBSL-V2 turbulence model, this increase does not seem a prohibitive cost for industrial applications. These results encourage the authors to improve these nonlinear eddy-viscosity turbulence models and validate them for a larger number of test cases in order to justify their integration into industrial routines.

Table 3: Computational cost estimates for the three turbulence models for the solution of the OAT15A airfoil flow using the fine mesh. The values are normalized by the cost of the SST solution.

SST	NLBSL	NLBSL-V2
1	1.12	1.13

4. CONCLUDING REMARKS

The current study aims to explore the application of nonlinear eddy-viscosity turbulence models in aeronautical contexts, with a focus on achieving computational costs suitable for daily engineering practices. The results obtained so far with the nonlinear turbulence models in the present investigation are very encouraging. The results for the flat plate test case indicate the correct implementation of the two nonlinear models in the current version of the code.

The compressibility effects present in the nonlinear formulation of the NLBSL-V2 turbulence model seem to be very important for achieving improved agreement on the shock wave position in the solution of transonic flow over the OAT15A airfoil. Besides providing better fidelity in the representation of the shock wave, the results have also indicated that these nonlinear turbulence models do not require much additional computational resources. Furthermore, although the NLBSL turbulence model results have not demonstrated any relevant improvements over those results obtained with the SST model, for the test cases addressed so far, the calculations of the additional test cases that are currently being addressed will continue to also consider this turbulence closure. This approach is being employed because there are other phenomena important to aeronautical applications besides transonic shock waves, and it is expected that the features of the NLBSL model could be relevant in other flight conditions.

This research will be continued with the aim of assessing the effects of using these nonlinear turbulence models on computing the aerodynamic coefficients in flows where the airfoil is at high angles of attack and high-lift flows, which are applications of interest of the aeronautical industry. It is important to emphasize that the computational cost estimates obtained for the 2-D test case of the transonic airfoil encourage the study of the nonlinear turbulence models in order to obtain more accurate representations of complex flows for industrial applications at acceptable costs.

5. ACKNOWLEDGEMENTS

The authors acknowledge the computational resources from the Center for Mathematical Sciences Applied to Industry, CeMEAI, funded by Fundação de Amparo à Pesquisa do Estado de São Paulo, FAPESP, under the Research Grant No. 2013/07375-0. Further support to the second author under the same FAPESP Grant is also acknowledged. The authors also acknowledge the support for the present work through a doctoral scholarship to the first author under the FAPESP Grant No. 2023/09177-2, associated to the Engineering Research Center for the Aerial Mobility of the Future, FLYMOV, funded by the FAPESP Grant No. 2021/11258-5. The authors further acknowledge the support for the present research provided by Conselho Nacional do Desenvolvimento Científico e Tecnológico, CNPq, under the Research Grant No. 315411/2023-6. Finally, the authors are also grateful for the support provided by Coordenação de Aperfeiçoamento do Pessoal de Nível Superior, CAPES, under the Grant No. 88887.799421/2022-00.

6. REFERENCES

Bigarella, E.D.V. and Azevedo, J.L.F., 2007. "Advanced eddy-viscosity and Reynolds-stress turbulence model simulations of aerospace applications". *AIAA Journal*, Vol. 45, No. 10, pp. 2369–2390.

Bigarella, E.D.V. and Azevedo, J.L.F., 2009. "A unified implicit CFD approach for turbulent-flow aerospace-configuration simulations". *47th AIAA Aerospace Sciences Meeting Including The New Horizons Forum and Aerospace Exposition,* AIAA Paper No. 2009-1473.

Bigarella, E.D.V. and Azevedo, J.L.F., 2012. "A study of convective flux schemes for aerospace flows". *Journal of the Brazilian Society of Mechanical Sciences and Engineering*, Vol. 34, No. 3, pp. 314–329.

Blazek, J., 2015. *Computational Fluid Dynamics: Principles and Applications*, Elsevier Science Ltd, Oxford. 3rd edition.

Carvalho, L.M.M.O., Almeida, A.C.V.M., Silva, R.G., Basso, E. and Azevedo, J.L.F., 2018. "Robust parallel computations of turbulent aerodynamic flows". *2018 AIAA Aerospace Sciences Meeting,* AIAA Paper No. 2018-1788.

Carvalho, L.M.M.O., da Silva, R.G. and Azevedo, J.L.F., 2019. "Numerical effects of flux calculation schemes for unstructured grid turbulent flow simulations". *AIAA Aviation 2019 Forum,* AIAA Paper No. 2019-2924.

Cary, A.W., Dorgan, A.J. and Mani, M., 2009. "Towards accurate flow predictions using unstructured meshes". *19th AIAA Computational Fluid Dynamics,* AIAA Paper No. 2009-3650.

Chagas Silva, T., 2021. *Nonlinear Eddy-Viscosity Turbulence Models for Simulations of Compressible Flows in Aeronautical Applications*. Master Thesis, Instituto Tecnológico de Aeronáutica, São José dos Campos, SP, Brazil (in portuguese).

Chagas Silva, T., Matunaga, M.A.L., da Silva, R.G. and Azevedo, J.L.F., 2022. "Numerical influence of viscous flux calculation schemes for turbulent flow simulations in aeronautical applications". *19th Brazilian Congress of Thermal Sciences and Engineering,* ENCIT Paper No. 2022-0046.

Eisfeld, B., Rumsey, C. and Togiti, V., 2016. "Verification and validation of a second-moment-closure model". *AIAA Journal*, Vol. 54, No. 9, pp. 1524–1541.

Gatski, T.B., Rumsey, C.L. and Manceau, R., 2007. "Current trends in modelling research for turbulent aerodynamic flows". *Philosophical Transactions of the Royal Society A: Mathematical, Physical and Engineering Sciences*, Vol. 365, No. 1859, pp. 2389–2418.

Hellsten, A., 2005. "New advanced k-ω turbulence model for high-lift aerodynamics". *AIAA Journal*, Vol. 43, No. 9, pp. 1857–1868.

Menter, F.R., 1993. "Zonal two equation k-ω turbulence models for aerodynamic flows". *24th Fluid Dynamics Conference,* AIAA Paper No. 93-2906.

Oliveira, F.B. and Azevedo, J.L.F., 2022. "On the influence of gradient reconstruction procedures over the accuracy of finite volume based schemes". *Proceedings of the 33rd Congress of the International Council of the Aeronautical Sciences*, ICAS Paper No. 2022-0191.

Oliveira, F.B. and Azevedo, J.L.F., 2023a. "Assessment of interface gradient reconstruction techniques for finite volume methods in aerospace applications". *AIAA AVIATION 2023 Forum,* AIAA Paper No. 2023-3241.

Oliveira, F.B. and Azevedo, J.L.F., 2023b. "A study of improved limiter formulations for second-order finite volume schemes applied to unstructured grids". *27th ABCM International Congress of Mechanical Engineering,* COBEM Paper No. 2023-0213.

Pope, S.B., 2000. *Turbulent Flows*, Cambridge University Press, chapter 7.

Roddle, A.M. and Archambaud, J.P., 1994. "A selection of experimental test cases for the validation of CFD codes". *NATO Advisory Group for Aerospace Research & Development,* AGARD-AR-303.

Roe, P.L., 1981. "Approximate Riemann solvers, parameter vectors, and difference schemes". *Journal of Computational Physics*, Vol. 43, pp. 357–372.

Rumsey, C., 2024. "Turbulence modeling resource web page". URL <https://turbmodels.larc.nasa.gov/> Last access: Jun. 2024.

Saad, Y. and Schultz, M.H., 1986. "GMRES: A generalized minimal residual algorithm for solving nonsymmetric linear systems". *SIAM Journal on Scientific and Statistical Computing*, Vol. 7, No. 3, pp. 856–869.

Spalart, P.R. and Allmaras, S.R., 1994. "A one-equation turbulence model for aerodynamic flows". *La Recherche Aeropastiale*, Vol. 1, pp. 5–21.

van Leer, B., 1979. "Towards the ultimate conservative difference scheme. V. A second-order sequel to Godunov's method". *Journal of Computational Physics*, Vol. 32, No. 1, pp. 101–136.

Wallin, S. and Johansson, A.V., 2000. "An explicit algebraic Reynolds stress model for incompressible and compressible turbulent flows". *Journal of Fluid Mechanics*, Vol. 403, pp. 89–132.

7. RESPONSIBILITY NOTICE

The authors are the only responsible for the printed material included in this paper.